

Different Transient Phenomena at the Edges of Traveling Foreshocks

Primož Kajdič^{1,*}, Xóchitl Blanco-Cano¹, Diana Rojas-Castllo¹ and , Nojan Omidi².

January 27, 2026

¹ Departamento de Ciencias Espaciales, Instituto de Geofísica, Universidad Nacional Autónoma de México, Mexico City, Mexico

² Solana Scientific Inc., Solana Beach, CA, USA

Abstract

Past kinetic simulations and spacecraft observations have shown that traveling foreshocks (TFs) are bounded by either foreshock compressional boundaries (FCBs) or foreshock bubbles (FBs). Here we present four TFs with a different kind of structure appearing at one of their edges. Two of them, observed by the Cluster mission, are bounded by a hot flow anomaly (HFA). In one case, the HFA was observed only by the spacecraft closest to the bow shock, while the other three probes observed an FCB. In addition, two other TFs were observed by the MMS spacecraft to be delimited by a structure that we call HFA-like FCB. In the spacecraft data, these structures present signatures similar to those of HFAs: dips in magnetic field magnitude and solar wind density, decelerated and deflected plasma flow and increased temperature. However, a detailed inspection of these events reveals the absence of heating of the SW beam. Instead, the beam almost disappears inside these events and the plasma moments are strongly influenced by the suprathermal particles. We suggest that HFA-like FCBs are related to the evolution and structure of the directional discontinuities of the interplanetary magnetic field whose thickness is larger than the gyroradii of suprathermal ions. We also show that individual TFs may appear together with several different types of transient upstream mesoscale structures, which brings up a question about their combined effect on regions downstream of the bow shock.

1 Introduction

The region upstream of the Earth’s bow shock is highly dynamic, hosting different phenomena. Among the former is our planet’s foreshock [12] that forms upstream of the quasi-parallel section of the bow shock, where the angle between the upstream interplanetary magnetic field (IMF) and the local normal to the shock, θ_{BN} , is less than 45° . In the foreshock, the pristine solar wind (SW) particles coexist with suprathermal ion populations that are leaked or reflected and energized by the bow shock. Depending on the location inside the foreshock, the suprathermal ions can appear in the form of field-aligned ion beams [FAB, e.g. 14, 39, 28], gyrating population [3, 16, 27] and diffuse ions [40, 7, 8, 58]. The interaction between the SW and the suprathermal ions leads to plasma and magnetic field instabilities and consequently to the formation of ultra-low frequency (ULF) waves. The most studied

among them are the so called 30-second waves [10, 11], which start out as quasi-monochromatic, transverse waves that are convected towards the bow shock by the SW. As they approach the bow shock, the ULF waves steepen and become more compressive [19, 31, 46, 18].

The foreshock is often observed to be delimited by a structure called the foreshock compressional boundary [FCB, e.g. 52, 35, 44]. FCBs separate the section of the foreshock populated by compressive ULF waves from either the pristine SW or from the region of the foreshock populated by FABs, but not by the ULF waves. Their signatures in the spacecraft data include a concurrent rise in the magnetic field magnitude and plasma density on the magnetically quiet side, followed by their depletion on the turbulent side. It has been shown in the past that FCBs affect regions downstream of the bow shock: they have been observed to cause local distortions of the magnetopause and transient magnetic field and plasma density perturbations in the magnetosphere [20].

Past spacecraft observations have revealed the presence of structures called foreshock cavities (FC) that form as a result of a small-scale magnetic flux tube of IMF lines connecting to a nominally quasi-perpendicular ($\theta_{BN} \geq 45^\circ$) section of the bow shock in a quasi-parallel manner [FC, e.g. 51, 5, 6]. According to [52], some FC signatures in the spacecraft data may appear due to a finite period in-and-out encounter of the spacecraft with the foreshock. To distinguish between the two possibilities [34] and [23] refer to FCs associated with flux tubes as traveling foreshocks (TF). In the spacecraft data, TFs exhibit all the signatures of a “normal” foreshock, however, they appear bounded by two IMF directional discontinuities, indicating crossing of the spacecraft from one magnetic flux tube into another. TFs have been shown to drive magnetospheric Pc1 and EMIC waves [55], cause transient compression in the dayside magnetosphere and are a source of magnetosheath jets in the quasi-perpendicular magnetosheath [53, 24].

Another type of structure commonly observed upstream of the bow shock are hot flow anomalies [HFA, 17, 41, 48, 30]. These occur when an IMF directional discontinuity intersects the bow shock and the convection electric field ($-\mathbf{V} \times \mathbf{B}$) points towards the discontinuity on at least one side. Then the ions reflected by the bow shock are channeled towards upstream along the discontinuity, heating the plasma and making it expand. HFAs can be observed upstream of a quasi-perpendicular bow shock as well as inside the foreshock.

In the spacecraft data, the HFAs exhibit a hot core inside which the B-magnitude and plasma density are strongly depleted and the plasma flow is decelerated and deflected. The core is delimited by leading and trailing edges on at least one side in which magnetic field strength and plasma density are enhanced. HFAs have been shown to cause the magnetopause displacement and magnetospheric perturbations [49, 57] and their effects on the geomagnetic field have been detected by ground based observatories [e.g., 50, 21, 15, 25].

In addition to HFAs, the presence of RDs and TDs in the solar wind and their interaction with the backstreaming ions in the foreshock can result in the generation of other transient phenomena, such as foreshock bubbles [FB, 33, 37, 36, 38]. In the hybrid simulations of [34] it was shown that depending on plasma conditions, the edge of a TF may be associated with an FB instead of an FCB. Spacecraft observations at Mars by [26] show an example of a traveling foreshock with an FB at one edge.

Foreshock compressional boundaries, traveling foreshocks, hot flow anomalies and foreshock bubbles are some of the types of transient upstream mesoscale structures [TUMS, 25] that are commonly observed upstream of the bow-shock of Earth. Their

typical scale sizes range from ~ 2000 km to more than 10 Earth radii ($1 R_E \sim 6400$ km) [60] and they are thought to play an important role in the processes that enable the transfer of the SW mass, momentum and energy into the magnetosphere of our planet.

In this work we show that HFAs may replace FCBs at the edges of TFs. This occurs when the motional electric field points towards the IMF directional discontinuities bounding these foreshocks. We present two TFs that exhibit HFAs on one of their edges. These were observed by the constellation of the Cluster spacecraft on 5 January 2005 (Section 3.1) and 12 January 2005 (Section 3.2).

We also show that on occasions, FCBs bounding TFs may have an HFA-like appearance in the spacecraft data. However, a more detailed analysis reveals that the apparently enhanced temperatures and decreased and deflected velocities in their cores do not stem from heating of the SW ion beam. In fact, there is no evidence for the SW beam heating inside these events and the beam is strongly reduced inside them. The measured plasma moments are heavily influenced by the suprathermal ions. The latter tend to be hotter and more diffuse than their counterparts inside the corresponding TFs. We feature two HFA-like FCBs observed by the MMS mission on 6 February 2022 (section 4.1) and on 30 January 2022 (Section 4.2).

In the following we describe the datasets used for the purpose of this study in Section 2, we feature the events in Sections 3 and 4 and discuss our findings in Section 5. Finally, we present our conclusions in Section 6.

2 Instruments and Data Sets

In this work we use observations from two multi-spacecraft missions: Cluster [13] and Magnetospheric Multiscale Mission [MMS, 9]. Both missions consist of four identical satellites that continuously measure magnetic field and plasma properties in the near-Earth environment.

The Cluster spacecraft carried several instrument suits. Here, we use the magnetic field data from the Fluxgate Magnetometer [FGM, 4] with a time resolution of 0.2 seconds. We also examine plasma data with a time resolution of ~ 4 seconds from the Hot Ion Analyser (HIA) instrument which forms part of the Cluster Ion Spectrometer [CIS, 43] package.

In the case of the MMS mission we use plasma data from the Fast Plasma Instrument [42] with a time resolution of 4.5 seconds and the magnetic field data from the Fluxgate Magnetometer [45] with a time resolution of 4.5 second and 1/16th of a second.

3 HFAs at the edges of traveling foreshocks

3.1 5 January 2005 event

The first event was observed on 5 January 2005 by the Cluster 1 (C1) spacecraft. Figure 1A exhibits an 11-minute time interval during which the TF with a HFA was observed. At $\sim 10:42$ UT, C1 entered the foreshock region marked by enhanced fluxes of suprathermal ions (orange, green and yellow colors with energies above ~ 8 keV on panel h). There were no 30 second (~ 0.03 Hz) ULF waves were present at that time (see panels a, b and the wavelet spectrum of the $B_{X,GSE}$ component on panel i), indicating that the observed suprathermal ions were FABs [e.g., 28], which we show

explicitly below. C1 did not detect any IMF directional discontinuity upon entering this region, which thus probably belongs to the “normal” foreshock of Earth.

At 10:45:57 UT C1 detected an IMF directional discontinuity that was followed by a region populated by compressive ULF fluctuations and different types of ion populations. Among the latter are the SW beam ions that have not been heated and are visible on the panel h as a continuous narrow yellow strip that is present throughout the entire exhibited time interval, suprathermal foreshock ions with energies above that of the SW beam that are present throughout the foreshock interval and locally heated SW ions with a much wider range of energies that also span below that of the SW beam. Concurrently with the discontinuity, C1 observes an FCB marked by initial rise in B and n values, followed by their drop compared to surroundings.

At \sim 10:47 UT the plasma velocity decreased from \sim 640 km s $^{-1}$ to 145 km s $^{-1}$, mainly due to the changes in V_x component (red shading in Figure 1A. The region of diminished SW speed occurs together with strong decreases in plasma density and the IMF magnitude and it is delimited by two rims with increased values of B and N. The parallel ion temperature (red trace panel d) there is enhanced from 1 MK to about 3 MK, while the perpendicular temperature exhibits no major variations. Due to these signatures and the fact that the magnetic field across it rotates by \sim 30°, we denote it as HFA0.

At the trailing edge of the traveling foreshock (\sim 10:50 UT, purple shading) we observe another event presented in more detail in Figure 1B. It exhibits a set of signatures typical of HFAs: a core with strongly diminished plasma density (almost to \sim 0) and highly fluctuating magnetic field that is bounded by two rims where both of these quantities are enhanced. In the core of this HFA, the parallel ion temperature (red trace) rises from \sim 0.5 MK to \sim 2.7 MK, while the perpendicular temperature (blue trace) jumps to \sim 3.8 MK. The SW velocity drops from 640 km s $^{-1}$ to 215 km s $^{-1}$ inside the core of the event, mainly due to the V_x component. Because of the strong drop in V and N, the dynamic pressure P_{dyn} also diminishes. The IMF rotates across the associated IMF directional discontinuity by \sim 37°. The ion spectrum (panel h) indicates that the temperature rise inside the HFA core is largely due to the strong heating of the pristine SW ion population.

In the Figure 1C we show the magnetic field profiles from all Cluster satellites. We can see that C2, C3 and C4 probes did not observe HFA signatures (enhanced rims, pronounced central dip). Additional inspection of the C3 plasma data (not shown) revealed lack of plasma heating indicating that these three probes probably observed an FCB or, alternatively a very young HFA. The reason for this can be inferred from Figure 2 where we show the locations of the Cluster probes during the detection of the HFA/FCB. At that time, the X_{GSE} coordinate of the C1 spacecraft was the smallest of all, indicating that this spacecraft was closest to the bow shock. This was verified by calculating the distances of all four spacecraft from the model bow shock described by [54] as a hyperboloid with eccentricity of 1.15, the location of the foci at (3,0,0) R_E and semi-latus rectum of 23.75 R_E . The latter value was obtained by scaling the original [54] model by using the ambient SW dynamic pressure values, as described in [22]. Thus, this mature HFA only stretched slightly beyond the C1 location but not all the way to the other probes.

All four spacecraft observed the directional discontinuity at the downstream edge of the traveling foreshock at slightly different times. We use the timing method similar to the one described by [47] to calculate the normal to the plane of the discontinuity. In the Figure 1D we present the B_y profiles from all Cluster satellites during the

time interval that contains the directional discontinuity. In order to calculate the normal, we use the times of a common feature that appears in the data of all four probes: the moment when the values of the B_y component start diminishing towards negative values (marked by arrows). The Figure 1D reveals that the order in which the probes detected this feature is C3 (red), C2 (blue), C1 (black) and C4 (green). The corresponding times were 10:49:55.461 UT, 10:49:54.517 UT, 10:49:54.265 UT and 10:49:55.902 UT, respectively. We calculate the normal vector to the discontinuity in the GSE coordinates to be $\hat{n} = (-0.81, 0.11, 0.57)$.

The direction of the normal is marked in the Figure 2 with a brown arrow, while the SW speed is represented with the magenta arrow.

We proceed by evaluating the type of the discontinuity, i.e. tangential versus rotational. We do so by calculating the following values from the C1 data and adopting the criteria from [29]:

$$B_n/B = 0.46, \quad (1)$$

$$\Delta B/B = 0.024, \quad (2)$$

where B_n is the component of the IMF normal to the discontinuity plane and the ΔB is the difference between the magnetic field magnitudes on both sides of the discontinuity. B is the magnitude that is equal to the larger of the two. According to the classification by [29] this discontinuity fulfills the criteria for a rotational discontinuity ($\Delta B/B < 0.2$ and $B_n/B \geq 0.4$).

We also check whether conditions for an HFA formation have been met by calculating the directions of the convection electric field ($-\mathbf{V} \times \mathbf{B}$) on both sides of the discontinuity. We use the C1 data averaged over a ~ 1 -minute time intervals.

Inside the traveling foreshock, the angle between the normal to the plane of the discontinuity and the convection electric field is equal to 106° , while outside it is 79° . Thus, the first condition for the formation of the HFA (convection electric field pointing towards the discontinuity on at least one side) is met.

We further analyze ion fluxes and velocity distribution functions (VDFs) during times when the traveling foreshock was observed. The Figure 3A shows magnetic field magnitude (a), ion spectra (f) and ion energy fluxes in four different energy ranges that correspond to ions with energies below the SW beam energy (b), the SW beam energies (c) and to suprathermal energy ranges (d and e). Vertical lines on the bottom panel indicate the times of the ion VDFs exhibited in Figure 3B.

The most notorious feature in the Figure 3A is the strong peak in the flux of ions with energies below that of the SW inside the HFA. The flux also peaks in the SW beam energy range (panel c), although the peak is less prominent compared to the rest of the TF interval. Ions in higher energy ranges (panels d and e) do not display any special behavior.

Figure 3B shows ion distributions inside the traveling foreshock and in its vicinity in the SW bulk rest frame. The left panels feature VDFs projected onto the (V_{per1}, V_{par}) plane, where V_{par} is the velocity component parallel to the background IMF, while V_{per1} direction is calculated as $-\mathbf{V} \times \mathbf{B}$, so it is parallel to the direction of the convection electric field. The right panels show VDFs in the (V_{per1}, V_{per2}) plane, where $V_{per2} = V_{par} \times V_{per1}$ (direction of electric field drift velocity). The described planes are chosen so that they contain the origin.

Figure 3Bi shows that before the arrival of the TF, there are two dominant ion populations: one that constitutes the SW wind beam (close to the origin of the two panels) and the second one with positive (sunward) parallel velocities, thus forming

a field-aligned ion beam (FAB). Figure 3Bii shows ion distributions just prior the HFA. The SW beam is still present, however there is a second population that forms a partial ring around the SW beam on the left panel of Figure 3Bii. The right panels show that the distribution is basically gyrotropic [16]. Thus, this population can be described as in a stage between gyrating and diffuse.

In the core of the HFA (3Biii), the SW beam and suprathermal VDFs cover a much wider range of velocities, revealing a strong heating of both populations. Finally, the Figure 3Biv shows the distribution inside the rear edge of the traveling foreshock. Besides very intense and anisotropic SW population, the VDF also exhibits the presence of suprathermal ions that form intermediate, gyrophase-bunched population [16]. After that time, the ion VDF becomes that of the pristine SW beam (not shown).

3.2 12 January 2005 event

Figure 4A shows the time interval containing a traveling foreshock observed on 12 january 2005. On its trailing edge there is an HFA. The B-magnitude inside its core diminishes to 1.6 nT and the plasma density almost to zero. The parallel and perpendicular temperatures increase from ~ 0.8 MK to >23 MK and the SW flow decelerates from 660 km s^{-1} to 420 km s^{-1} . This is mainly due to the change of the V_x component, although the other two also exhibit significant change inside the HFA. The ion spectrum also shows ion heating in the core of the HFA. This time, all four Cluster probes observed the HFA.

Figure 4B exhibits B_y profiles during the second directional discontinuity from the four Cluster probes. We can see that the order in which the spacecraft detected it was C3, C4, C2 and C1. The time delays with respect to the C1 satellite were -4.8 s, -4.76 s and -4.65 s for C2, C3 and C4, respectively. Figure 4C exhibits the locations of the four Cluster probes at the time when they detected the HFA.

From the timing method we obtain the normal to the plane of the discontinuity to be $\hat{n} = (-0.51, -0.64, -0.57)$.

The angles between the normal to the discontinuity plane and the convection electric field inside and outside the traveling foreshock are 44° and 76° , which means that the HFA formation condition is met. Again, we calculate the quantities $B_n/B = 0.15$ and $\Delta B/B = 0.12$.

According to [29], the true character of such a discontinuity cannot be unambiguously determined, and the discontinuity could be either rotational or tangential.

We show ion fluxes in Figure 5A. It is clear that the fluxes below the SW energies (panel b) are strongly enhanced inside the HFA. Fluxes in the SW beam energy range (c) diminish compared to those just before the HFA. Suprathermal ions show a distinct peak just above the SW energies (d) and a less prominent one in the highest energy range (e).

In Figure 5B we show ion distributions at four selected times. Panel i) shows ion VDFs before the arrival of the traveling foreshock when only the SW ions are present. Later, well inside the foreshock (panel ii), there exists another, an almost completely diffuse ion population. Inside the HFA core (panel iii), the suprathermal ions exhibit intermediate-type of distribution, their VDF also appears more intense and hotter than inside the TF. Inside the rear rim of the HFA (panel iv) the ions form a gyrophase-bunched population [16].

4 HFA-like foreshock compressional boundaries

In this section we present two events that exhibit many of the observational signatures of HFAs, however a careful inspection reveals the absence of the SW beam heating in their cores.

4.1 6 February 2022 event

Our third case study consists of an event that was observed by the MMS spacecraft on 6 February 2022. At first glance, its signatures in Figure 6A and B) are similar to the HFAs: it appears at the downstream edge of a traveling foreshock and is centered on an IMF directional discontinuity. It exhibits strong temperature rise in the core of the event (to ~ 16.5 MK) and the flow is significantly deflected and decelerated from ~ 500 km s $^{-1}$ to ~ 240 km s $^{-1}$. The minimum B value inside the structure is only ~ 0.16 nT and the density falls to ~ 0.24 cm $^{-3}$.

This event, however, is different from the previous ones. The detailed inspection of the ion spectra in Figure 6Bh reveals that the SW wind beam does not undergo any heating at all. Rather, its intensity is strongly diminished and suprathermal ions are dominant in the core of the event.

We present ion energy fluxes in Figure 7A. We can see that the ion fluxes in the energy range below the pristine SW beam inside the structure are similar to those in the traveling foreshock, while in the energy range of the SW beam they diminish greatly. Suprathermal ions energy fluxes exhibit peaks inside the event.

We exhibit the ion distributions associated with this event in Figure 7B. Their times are indicated in Figure 7Af. Before the arrival of the traveling foreshock (panel i), there seem to be two ion populations present. The detailed inspection of the ion spectra and of the moments provided by Hot Plasma Composition Analyzer [HPCA, 59, not shown] reveal that both populations belong to the pristine SW beam. The one with \sim zero velocity in Figure 7Bi is formed by protons, while the other one by alpha (He $^{++}$) particles.

At the front rim of the event (panel ii) the two SW populations are joined by a hotter population which appears detached from them. In the core of the event (panel iii) the suprathermal population is hotter and almost completely diffuse, while the SW beam intensity is strongly diminished. After the event (panel iv), the suprathermal population is almost completely diffuse however colder than the one inside the event.

4.2 30 January 2022 event

Our last case study was observed on 30 January 2022 by the MMS mission (Figures 8A and B). The corresponding traveling foreshock was first detected at $\sim 20:10$ UT and it lasted until $\sim 20:25$ UT. The HFA-like event on its rear edge lasted from $\sim 20:23:45$ UT until 20:25:37 UT. The lowest B value inside it is almost 0 nT, while the lowest density value is 0.35 cm $^{-3}$. The temperature inside it peaks at 10.6 MK, while the SW speed drops from 433 km s $^{-1}$ inside the foreshock to the minimum value of 310 km s $^{-1}$ inside the event.

We again analyze the ion fluxes in and in the vicinity of this structure in Figure 9A. We see that the flux of ions with energies below that of the SW (b) exhibit similar levels to those inside the traveling foreshock. The fluxes in the SW beam range (c) decrease strongly inside the event, while the suprathermal ion fluxes (d and e) exhibit distinct peaks.

From Figure 9B we also see that the SW ion population significantly decreases in the core of the structure (9Biii). The VDFs of suprathermal ions change from intermediate before the event (9Bi) and in the front rim of the structure (9Bii), to a hot, diffuse population in the core of the event (9Biii). At later times (9B)iv) the pristine SW beam is dominant.

5 Discussion

5.1 Multi-TUMS events

It is already known that foreshocks, the “regular” and traveling, are commonly delimited by FCBs. However, TFs differ from the regular foreshock in that they form inside magnetic field flux tubes that connect to the nominally quasi-perpendicular shock in a quasi-parallel manner. Thus, in the spacecraft data, TFs are always bounded by IMF directional discontinuities. It seems natural that when the conditions are right, HFAs will appear instead of FCBs.

Such HFAs will, however, replace FCBs only along the section of the directional discontinuity close to the bow shock. This is because they will start to grow in the vicinity of the shock and will only gradually expand towards upstream. This might have been the case for the 5 January 2005 HFA that was observed only by the C1 spacecraft, while the three more distant probes detected an FCB.

Additionally, at the front edge of this TF the Cluster spacecraft observed an HFA-like FCB, while in its interior an HFA was detected. This means that four different TUMS (TF, HFA-like FCB, HFA and the trailing FCB) were impacting the bow shock almost simultaneously. The impact of such a multi-TUMS event will be a subject of future investigations.

Such studies are important, since there exist only a handful of investigations that deal with multi-TUMS events. [36], [36] and [56] performed 3- and 2.5-D hybrid simulations in order to show that a single IMF discontinuity can result in generation of FBs and HFAs. In the simulations by [37] both of these structures impact the magnetosheath of Venus resulting in the sunward expansion of the ionosphere and outflow of planetary ions with FB having a more global impact. In the simulations by [56] a single IMF directional discontinuity first drove an FB and later, upon intersecting the simulated Earth’s bow shock, it also lead to the formation of multiple HFAs. The combined impact of such multiple event on the bow shock and the downstream regions has not yet been investigated but [56] suggested that it is likely more intense than the impact of each individual structure.

5.2 HFA-like FCBs at the edges of traveling foreshocks

In the second part of our work we describe two TFs that present HFA-like FCBs at one of their edges. In the spacecraft data these events exhibit signatures similar to HFAs: a strong decrease of B and plasma density inside their cores that are accompanied by decelerated and deflected SW flows and a strong increase of temperature. However, a more detailed inspection reveals that in reality, the SW ions are not heated inside these events. The apparent temperature rise occurs mainly due to the fact that the SW ions there are almost absent and the plasma moments are strongly influenced by the suprathermal ion population. The latter, however, is hotter and more diffuse than the suprathermal ions in the rest of the TFs, resulting in a higher temperature.

Additionally, both HFA-like FCBs exhibit relatively modest rims, with small increases of B and N, and their profiles are quite “clean”, i.e. without large-amplitude B and N oscillations or waves inside them.

It is not clear at this point whether HFA-like FCBs are a new phenomenon that does not form due to explosive expansion, thus explainig the lack of active ion heating in their cores and weak rims, or whether they represent late phases of HFA evolution, whent the SW beam has been completely energized and converted into the suprathermal ion population and the expansion had slowed down and the rims had weakened.

An important difference between the IMF directional discontinuities associated with our first two case studies (the HFAs) and the last two events (HFA-like FCBs) is their duration in the spacecraft data. These were 38 seconds and 24 seconds for the 5 January 2005 and the 12 January 2005 events, respectively, and approximately 3 minutes and 15 seconds for the other two events.

We determined the thicknesses of the latter IMF directional discontinuities from their durations in the data and by calculating their normals using the cross product of the magnetic field vectors inside the TFs and in the pristine SW. The thicknesses were found to be $1.9 R_E$ and $1.6 R_E$ for the 6 February 2022 and the 30 January 2022 events, respectively. This is much more than the estimated Larmour radii of suprathermal ions in the 10 keV–30 keV energy range for both events that span between $0.37 R_E$ and $0.75 R_E$. Thus, it is safe to say that the two IMF rotations were so thick that the suprathermal ions have remained magnetized inside them.

This may be one of the reasons for why FB or HFA did not evolve at the edges of these TFs. [2] and [1] suggest that in order for these structures to form, the IMF rotations need to occur on spatial scales shorter than the gyro-radius of suprathermal ions. Thus, we turn to the work of [34] in order to try to find an explanation for the observed HFA-like FCBs.

[34] use a 2.5-D (2-D in space and 3-D in currents and electromagnetic fields) global hybrid code in order to study the dynamics of FCBs. The authors performed several runs under steady and time-varying IMF directions. In their second run, [34] simulate FCBs delimiting a traveling foreshock (see their Figure 6). The FCB that forms at the TF’s leading edge exhibits similarities with our observed events: dips in B and N profiles are much deeper than the amplitudes of the ULF waves and the temperature in the core of that structure is higher than in the rest of the TF.

To elaborate further, we show additional results from that run in Figure 10. Panels (a)-(e) exhibit respectively, variations of temperature (normalized to upstream value), ion velocity (normalized to Alfen speed), and magnetic field components and magnitude and density (normalized to upstream values) along a trajectory near the bow shock. Starting in the SW, one encounters the RD (purple shading) which is associated with an increase in temperature, small drop in velocity and large decreases in magnetic field and density. The rear part of the RD coincides with enhancements in magnetic field and density which are associated with the formation of the FCB (encased within the red rectangle). As is evident in Figure 6 of [34], the strength of the density enhancement associated with FCB decreases with distance from the bow shock (see panels (i) and (j) of Figure 10).

In general, the formation and properties of the FCB are not expected to be tied to the properties of the RD but related to the plasma conditions noted in [32, 34] such as the SW Mach number and the cone angle. Accordingly, we examine the properties of the RD by itself. In regards to the initialization of the RDs in the simulation, rotations in the magnetic field are implemented with a thickness of 2 thermal proton

inertial lengths without any changes in plasma properties. With time, the thickness of RDs adjusts to reach a self-consistent structure which does not look like that seen in panels (a-e) in Figure 10. To illustrate this point, panels (f-j) in Figure 10 show variations across the same RD as in panels (a)-(e) but at large distances from the bow shock. In contrast to the changes seen near the bow shock, except for some broadening and small drops in B within the RD no other changes are observed.

6 Conclusions

In this paper, we have examined the structure of the boundaries between TFs and the solar wind. Given that TFs are bounded by IMF RDs on both sides, the boundaries must include RDs as part of their structure. Past simulations and observations have shown that the edges of TFs may be associated with FCBs or FBs. In this study we show that TFs may also be associated with HFAs or nonlinear structures associated with the interaction of the RDs with the backstreaming ions from the bow shock. Past investigations have shown that formation of FCBs, HFAs and FBs all require certain plasma conditions which may or may not be met at the edges of a given TF. Accordingly, the edges of TFs, may be associated with any of these structures depending on the upstream conditions. We have also demonstrated that the interaction of RDs and backstreaming ions results in major changes in the properties of the RD including substantial decreases in density and magnetic field strength. This in turn impacts the overall structure of the TFs. Future work will show what is the impact if such structures on the bow shock and the regions downstream of it.

7 Acknowledgments

TP.K.'s work was funded by the PAPIIT-DGAPA through the project grant IN100424. DRC's work was supported by the UNAM-PAPIIT IA105223 grant and SECIHTI CF-2023-I-1264 grant. N.O.'s work at Solana Scientific Inc. was supported by the NASA-LWS grant #80NSCC23K1401. XBC acknowledges DGAPA PAPIIT grant IN106724.

References

- [1] Xin An, Terry Z. Liu, Jacob Bortnik, Adnane Osmane, and Vassilis Angelopoulos. Formation of Foreshock Transients and Associated Secondary Shocks. *The Astrophysical Journal*, 901(1):73, September 2020. doi: 10.3847/1538-4357/abaf03.
- [2] M. O. Archer, D. L. Turner, J. P. Eastwood, S. J. Schwartz, and T. S. Horbury. Global impacts of a Foreshock Bubble: Magnetosheath, magnetopause and ground-based observations. *Planet. Space Sci.*, 106:56–66, February 2015. doi: 10.1016/j.pss.2014.11.026.
- [3] H. V. Argo, J. R. Asbridge, S. J. Bame, A. J. Hundhausen, and I. B. Strong. Observations of solar wind plasma changes across the bow shock. *Journal of Geophysical Research (1896-1977)*, 72(7):1989–1994, 1967. doi: <https://doi.org/10.1029/JZ072i007p01989>. URL <https://agupubs.onlinelibrary.wiley.com/doi/abs/10.1029/JZ072i007p01989>.
- [4] A. Balogh, C. M. Carr, M. H. Acuña, M. W. Dunlop, T. J. Beek, P. Brown, K.-H. Fornacon, E. Georgescu, K.-H. Glassmeier, J. Harris, G. Musmann, T. Oddy, and K. Schwingenschuh. The cluster magnetic field investigation: overview of in-flight performance and initial results. *Annales Geophysicae*, 19(10/12):1207–1217, 2001. doi: 10.5194/angeo-19-1207-2001. URL <https://www.ann-geophys.net/19/1207/2001/>.
- [5] L. Billingham, S. J. Schwartz, and D. G. Sibeck. The statistics of foreshock cavities: results of a Cluster survey. *Ann. Geophys.*, 26:3653–3667, November 2008. doi: 10.5194/angeo-26-3653-2008.
- [6] L. Billingham, S. J. Schwartz, and M. Wilber. Foreshock cavities and internal foreshock boundaries. *Planet. Space Sci.*, 59:456–467, May 2011. doi: 10.1016/j.pss.2010.01.012.
- [7] C. Bonifazi and G. Moreno. Reflected and diffuse ions backstreaming from the earth’s bow shock 1. Basic properties. *Journal of Geophysical Research*, 86(A6):4397–4404, June 1981. doi: 10.1029/JA086iA06p04397.
- [8] C. Bonifazi and G. Moreno. Reflected and diffuse ions backstreaming from the earth’s bow shock 2. Origin. *Journal of Geophysical Research*, 86(A6):4405–4414, June 1981. doi: 10.1029/JA086iA06p04405.
- [9] J. L. Burch, R. B. Torbert, T. D. Phan, L. J. Chen, T. E. Moore, R. E. Ergun, J. P. Eastwood, D. J. Gershman, P. A. Cassak, M. R. Argall, S. Wang, M. Hesse, C. J. Pollock, B. L. Giles, R. Nakamura, B. H. Mauk, S. A. Fuselier, C. T. Russell, R. J. Strangeway, J. F. Drake, M. A. Shay, Yu. V. Khotyaintsev, P. A. Lindqvist, G. Marklund, F. D. Wilder, D. T. Young, K. Torkar, J. Goldstein, J. C. Dorelli, L. A. Avanov, M. Oka, D. N. Baker, A. N. Jaynes, K. A. Goodrich, I. J. Cohen, D. L. Turner, J. F. Fennell, J. B. Blake, J. Clemons, M. Goldman, D. Newman, S. M. Petrinec, K. J. Trattner, B. Lavraud, P. H. Reiff, W. Baumjohann, W. Magnes, M. Steller, W. Lewis, Y. Saito, V. Coffey, and M. Chandler. Electron-scale measurements of magnetic reconnection in space. *Science*, 352:aaf2939, Jun 2016. doi: 10.1126/science.aaf2939.

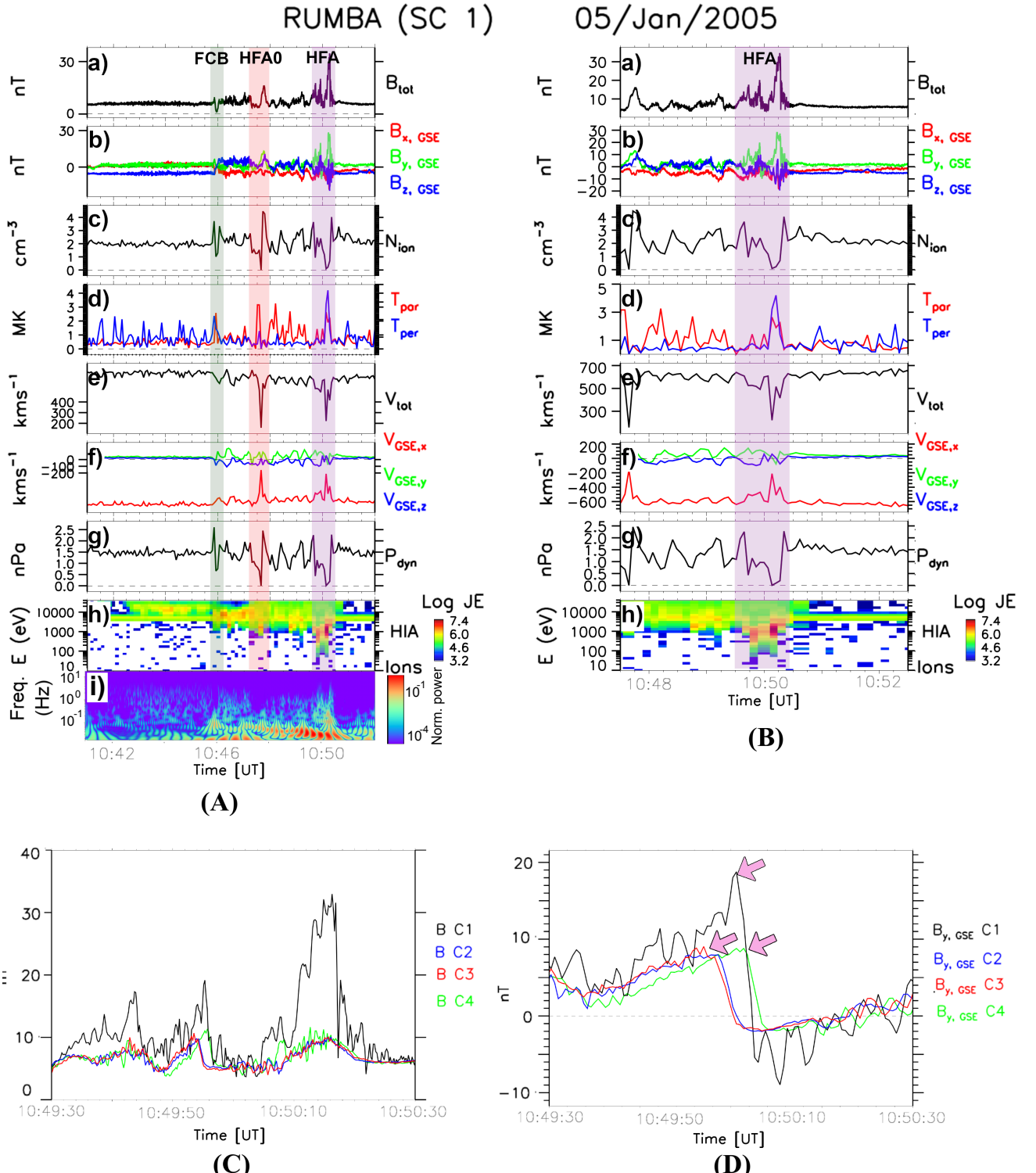


Figure 1: (A) Traveling foreshock observed on 5 January 2005 by the Cluster 1 spacecraft. Two events with major solar wind flow deceleration are associated to it. The first is a SHFA which was detected at 10:47 UT deep inside the traveling foreshock (red shading). The second event is an HFA detected at \sim 10:50 UT at the edge of the traveling foreshock (purple shading). (B) A shorter time interval centered on the HFA. Panels in Figures (A) and (B) exhibit (from top to bottom) IMF magnitude, IMF components in GSE coordinate system, plasma density, perpendicular (blue) and parallel (red) temperatures, SW bulk speed, SW velocity components in GSE coordinate system, dynamic pressure and ion spectrum. Additionally, panel Ai exhibits a Morlet wavelet spectrum of the $B_{x,\text{GSE}}$ component. (C) Magnetic field profiles of the four Cluster spacecraft during the HFA. (D) B_y profiles of the IMF

05 January 2005

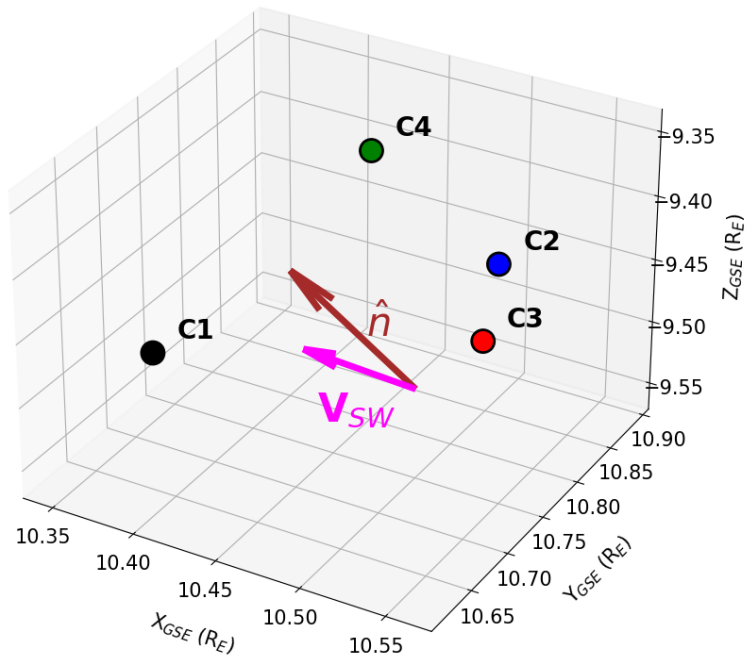


Figure 2: Locations of the Cluster probes during the detection of the IMF directional discontinuity on 5 January 2005. The brown arrow represents the vector normal to the directional discontinuity while the magenta arrow indicates the direction of the SW velocity.

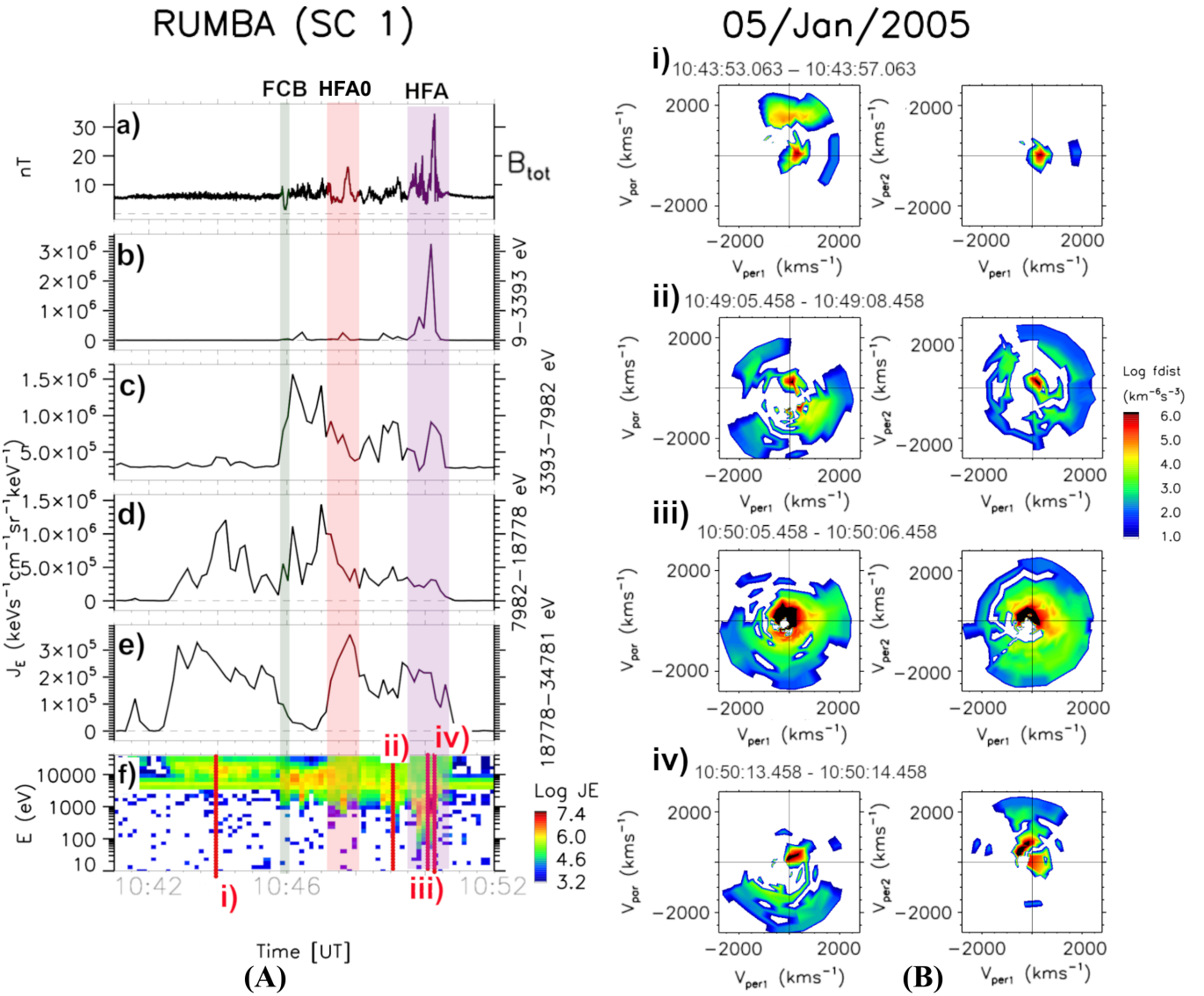


Figure 3: (A) From top to bottom: magnetic field magnitude, ion fluxes in different energy ranges and ion spectra during the time period when the traveling foreshock on 5 January 2005 was observed. (B) Ion distribution functions at selected times (marked in Figure 3Af).

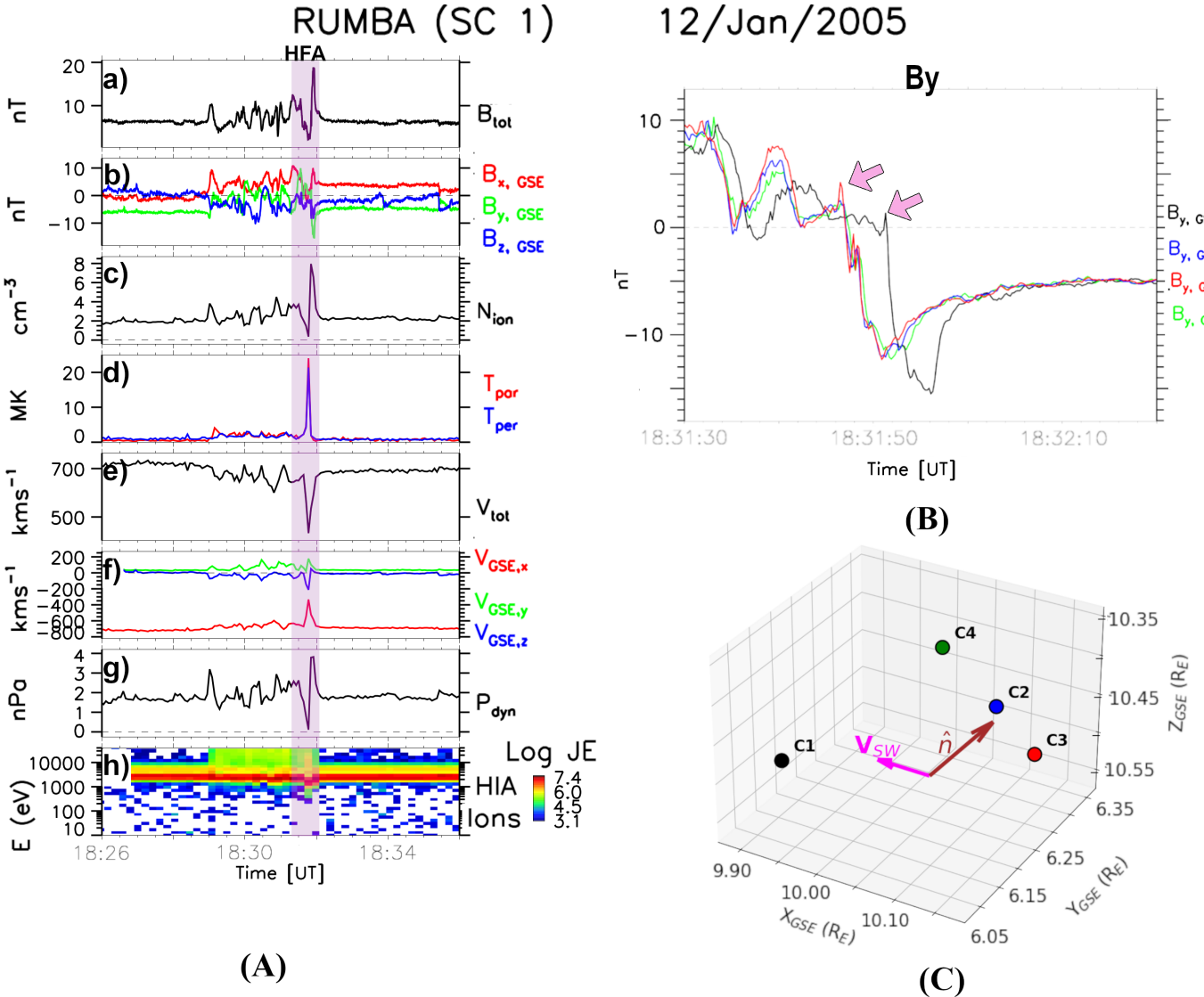


Figure 4: (A) Cluster 1 observations of a traveling foreshock with an HFA on its rear edge observed on 12 January 2005. (B) B_y profiles of the rear edge of the traveling foreshock. The arrows mark the times used in the timing analysis. (C) Positions of the Cluster probes during the detection of the IMF directional. The brown arrow represents the vector normal to the directional discontinuity while the magenta arrow indicates the direction of the SW velocity.

HIA RUMBA (SC 1) 12/Jan/2005

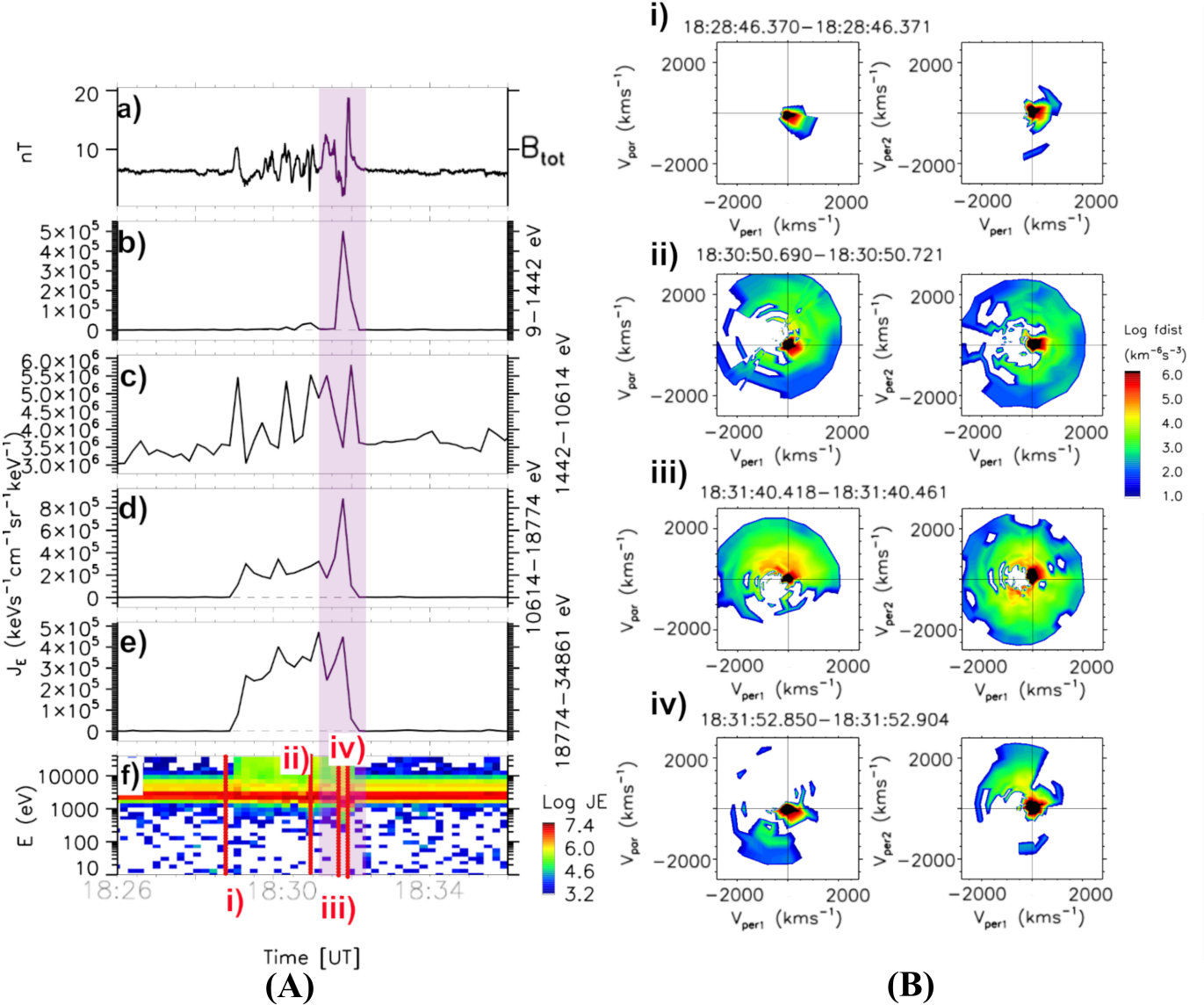


Figure 5: (A) Ion fluxes around the time of the 12 January 2005 event. (B) Ion distribution functions at selected times (marked in Figure 5Af).

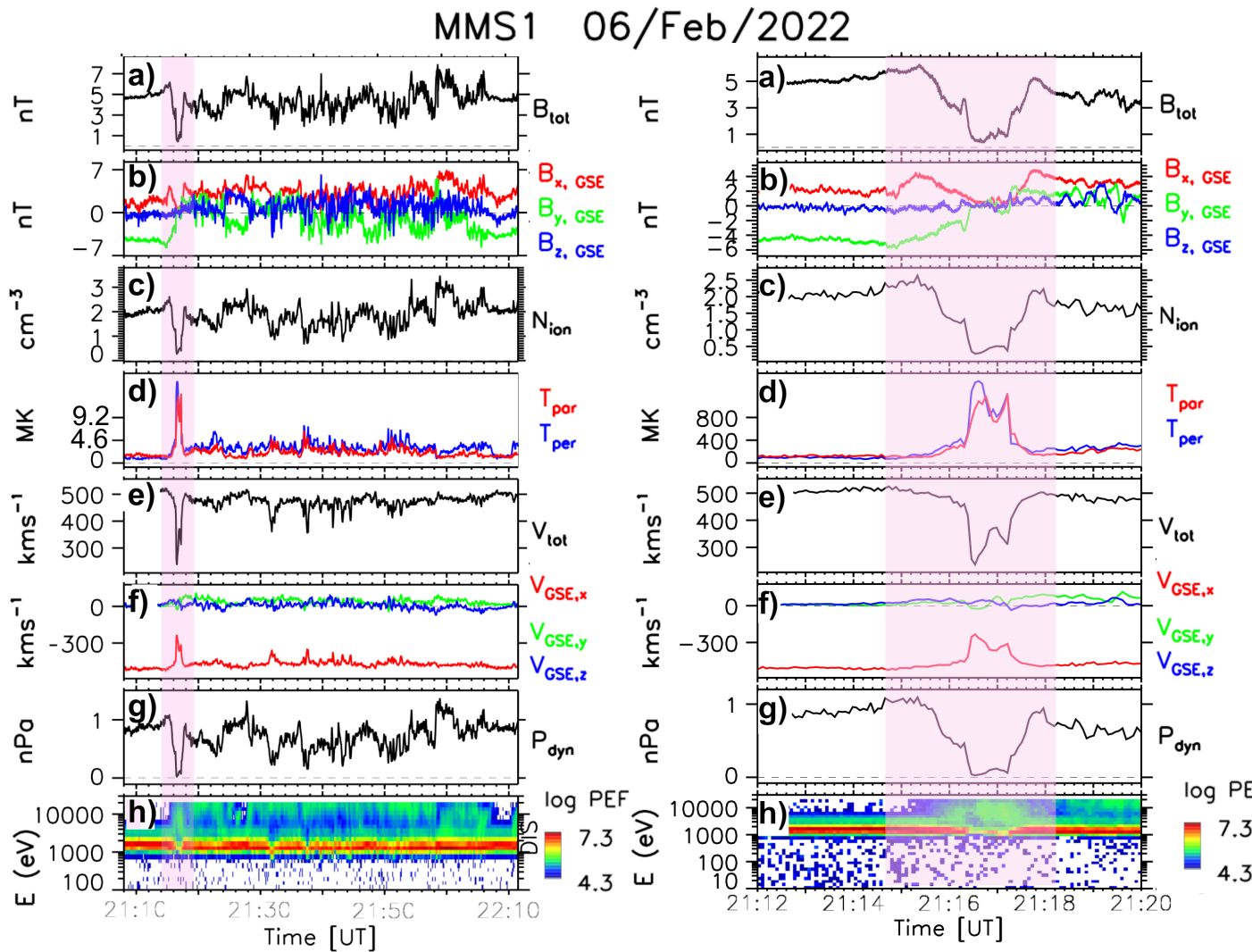


Figure 6: Traveling foreshock and HFA-like event observed on 6 February 2022.

MMS1 06/Febr/2022

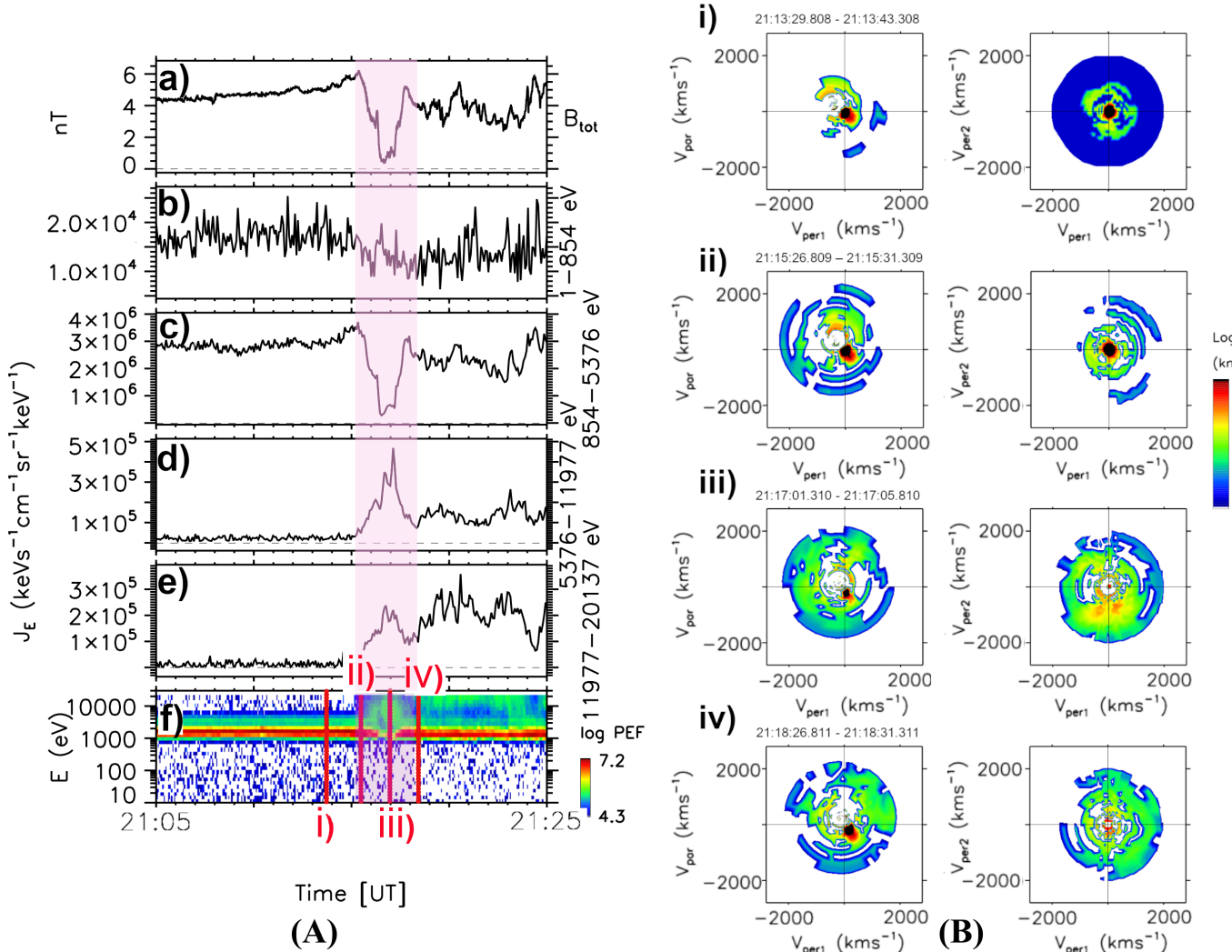


Figure 7: (A) Magnetic field and ion fluxes during the event observed on 6 February 2022. (B) on distribution functions at selected times marked in 7Af).

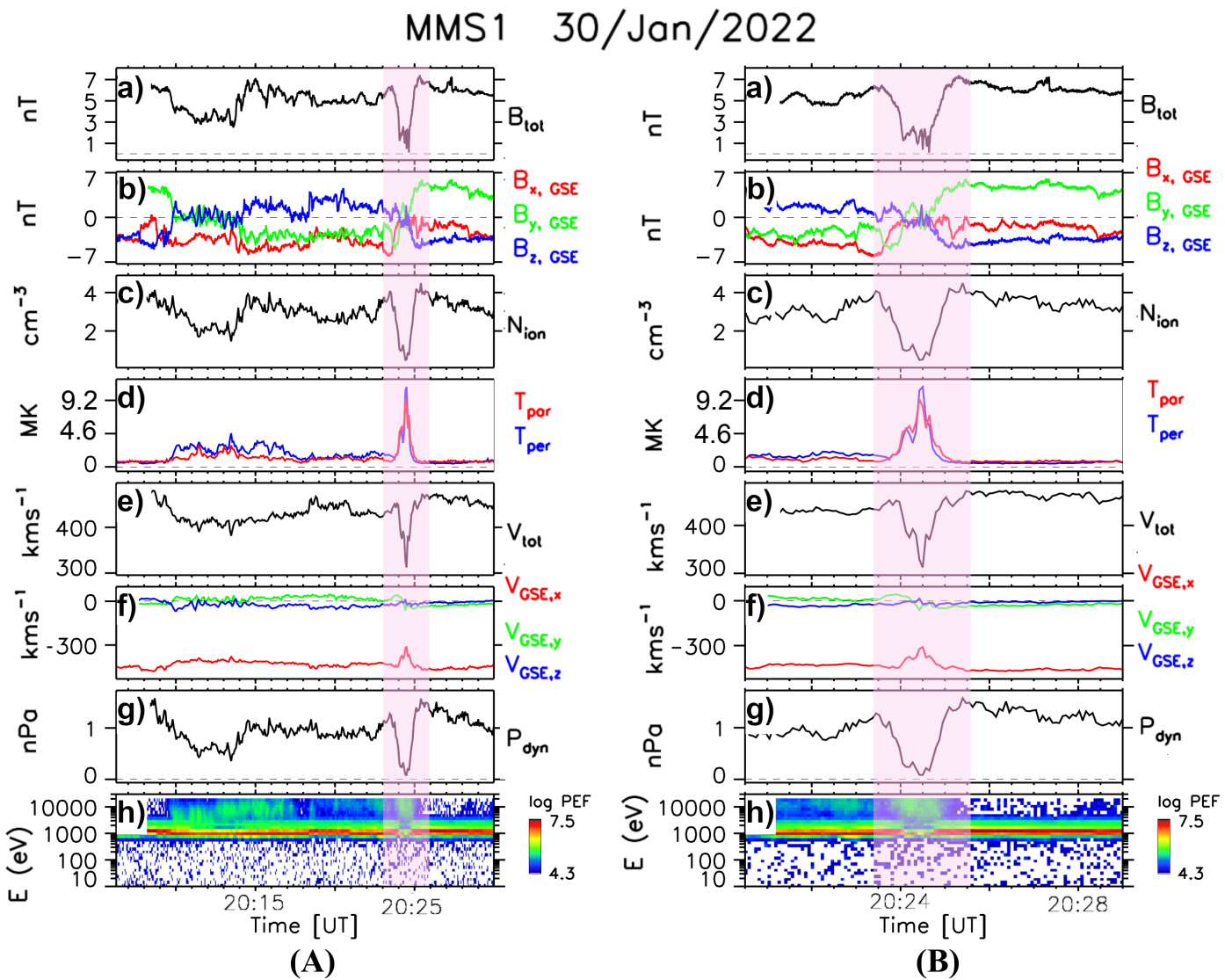


Figure 8: Traveling foreshock and HFA-like event observed on 30 January 2022.

MMS1 30/Jan/2022

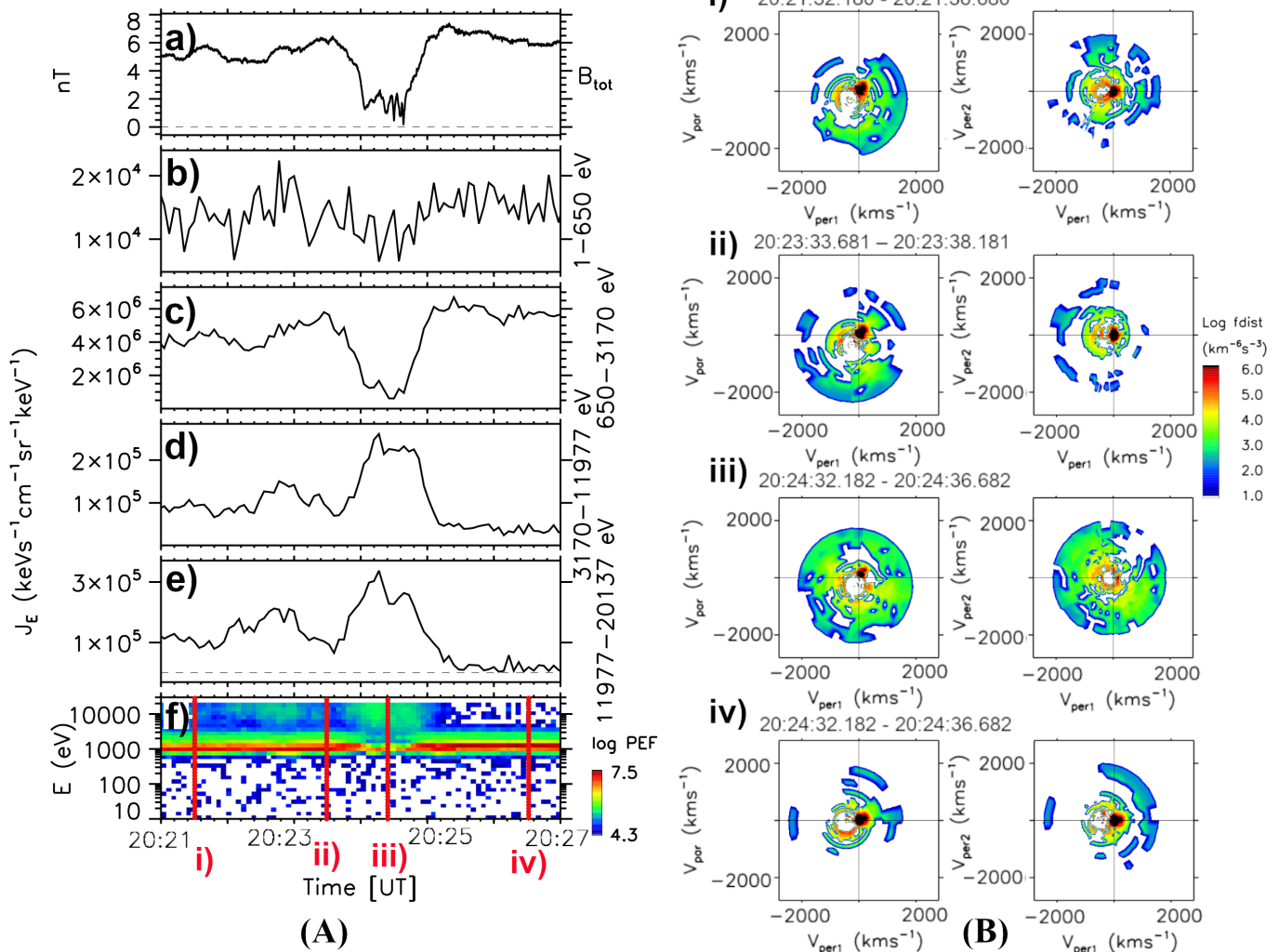


Figure 9: (A) Magnetic field and ion fluxes during the event observed on 6 February 2022. (B) on distribution functions at selected times marked in 9Af).

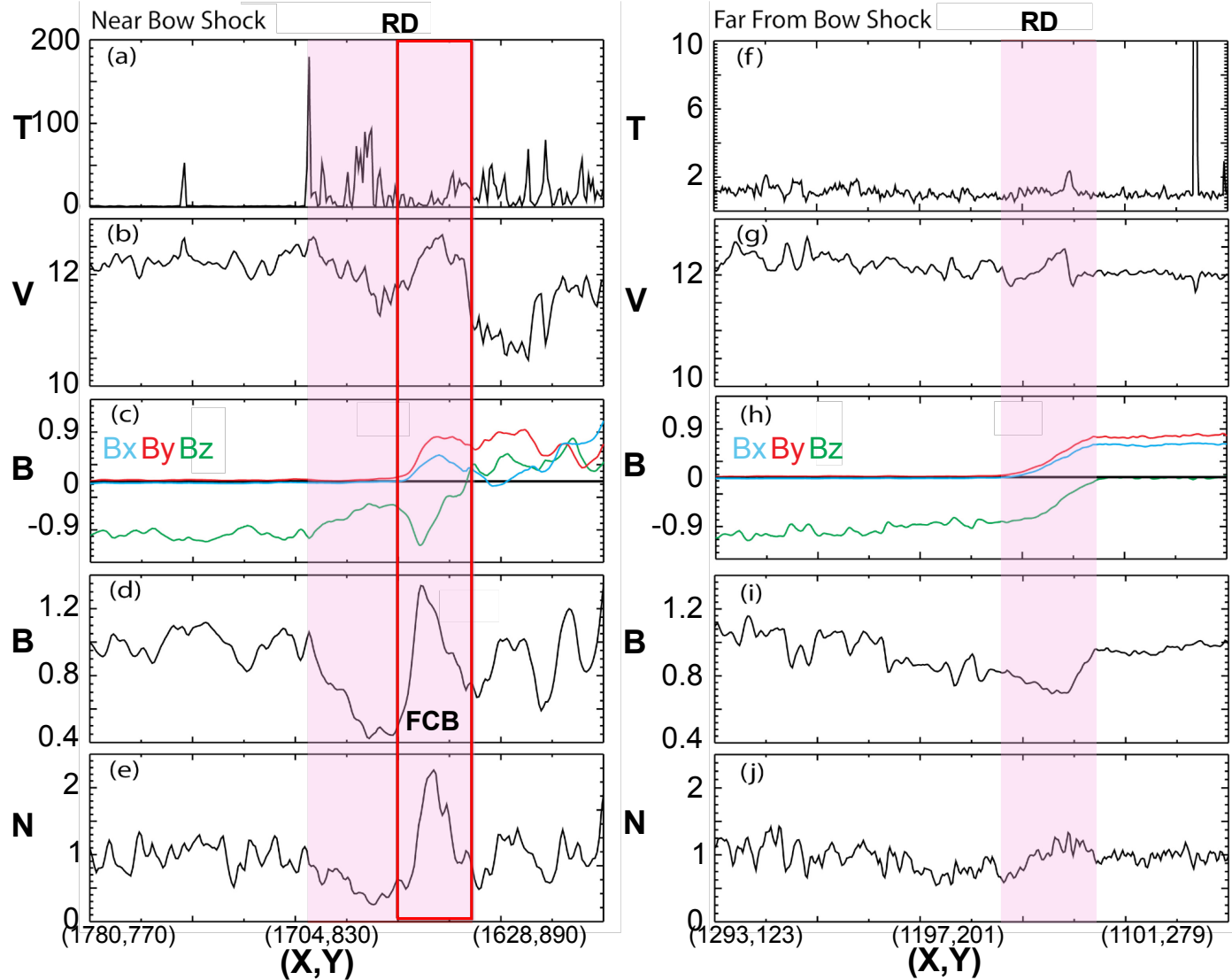


Figure 10: Simulations results from [34]. Panels show profiles of (from top to bottom) temperature, ion velocity, IMF magnitude and components and plasma number density close to the bow shock (left column) and farther away from the simulated bow shock (right column).

- [10] J. P. Eastwood, A. Balogh, E. A. Lucek, C. Mazelle, and I. Dandouras. Quasi-monochromatic ulf foreshock waves as observed by the four-spacecraft cluster mission: 1. statistical properties. *Journal of Geophysical Research: Space Physics*, 110(A11):n/a–n/a, 2005. ISSN 2156-2202. doi: 10.1029/2004JA010617. URL <http://dx.doi.org/10.1029/2004JA010617>. A11219.
- [11] J. P. Eastwood, A. Balogh, E. A. Lucek, C. Mazelle, and I. Dandouras. Quasi-monochromatic ulf foreshock waves as observed by the four-spacecraft cluster mission: 2. oblique propagation. *Journal of Geophysical Research: Space Physics*, 110(A11), 2005. doi: <https://doi.org/10.1029/2004JA010618>. URL <https://agupubs.onlinelibrary.wiley.com/doi/abs/10.1029/2004JA010618>.
- [12] J. P. Eastwood, E. A. Lucek, C. Mazelle, K. Meziane, Y. Narita, J. Pickett, and R. A. Treumann. The Foreshock. *Space Science Reviews*, 118(1-4):41–94, June 2005. doi: 10.1007/s11214-005-3824-3.
- [13] C. P. Escoubet, M. Fehringer, and M. Goldstein. Introduction The Cluster mission. *Annales Geophysicae*, 19:1197–1200, October 2001. doi: 10.5194/angeo-19-1197-2001.
- [14] D. H. Fairfield. Bow shock associated waves observed in the far upstream interplanetary medium. *Journal of Geophysical Research*, 74:3541, 1969. doi: 10.1029/JA074i014p03541.
- [15] M.O. Fillingim, J.P. Eastwood, G.K. Parks, V. Angelopoulos, I.R. Mann, S.B. Mende, and A.T. Weatherwax. Polar uvi and themis gmag observations of the ionospheric response to a hot flow anomaly. *Journal of Atmospheric and Solar-Terrestrial Physics*, 73(1):137–145, 2011. ISSN 1364-6826. doi: <https://doi.org/10.1016/j.jastp.2010.03.001>. URL <https://www.sciencedirect.com/science/article/pii/S1364682610000738>.
- [16] S. A. Fuselier. Ion distributions in the Earth’s foreshock upstream from the bow shock. *Advances in Space Research*, 15(8-9):43–52, January 1995. doi: 10.1016/0273-1177(94)00083-D.
- [17] S. A. Fuselier, M. F. Thomsen, J. T. Gosling, S. J. Bame, C. T. Russell, and M. M. Mellott. Fast shocks at the edges of hot diamagnetic cavities upstream from the Earth’s bow shock. *J. Geophys. Res.*, 92:3187–3194, 1987. doi: 10.1029/JA092iA04p03187.
- [18] E. W. Greenstadt, G. Le, and R. J. Strangeway. ULF waves in the foreshock. *Adv. Space Res.*, 15:71–84, 1995. doi: 10.1016/0273-1177(94)00087-H.
- [19] T. Hada, C. F. Kennel, and T. Terasawa. Excitation of compressional waves and the formation of shocklets in the earth’s foreshock. *J. Geophys. Res.*, 92: 4423–4435, May 1987. doi: 10.1029/JA092iA05p04423.
- [20] M. D. Hartinger, D. L. Turner, F. Plaschke, V. Angelopoulos, and H. Singer. The role of transient ion foreshock phenomena in driving Pc5 ULF wave activity. *Journal of Geophysical Research (Space Physics)*, 118:299–312, January 2013. doi: 10.1029/2012JA018349.
- [21] K. S. Jacobsen, T. D. Phan, J. P. Eastwood, D. G. Sibeck, J. I. Moen, V. Angelopoulos, J. P. McFadden, M. J. Engebretson, G. Provan, D. Larson, and

K.-H. Fornaçon. THEMIS observations of extreme magnetopause motion caused by a hot flow anomaly. *J. Geophys. Res.*, 114:A08210, August 2009. doi: 10.1029/2008JA013873.

[22] K. Jelínek, Z. Němeček, and J. Šafránková. A new approach to magnetopause and bow shock modeling based on automated region identification. *Journal of Geophysical Research (Space Physics)*, 117(A5):A05208, May 2012. doi: 10.1029/2011JA017252.

[23] P. Kajdič, X. Blanco-Cano, N. Omidi, D. Rojas-Castillo, D. G. Sibeck, and L. Billingham. Traveling foreshocks and transient foreshock phenomena. *Journal of Geophysical Research: Space Physics*, 122(9):9148–9168, 2017. ISSN 2169-9402. doi: 10.1002/2017JA023901. URL <http://dx.doi.org/10.1002/2017JA023901>. 2017JA023901.

[24] Primož Kajdič, Savvas Raptis, Xóchitl Blanco-Cano, and Tomas Karlsson. Causes of jets in the quasi-perpendicular magnetosheath. *Geophysical Research Letters*, 48(13):e2021GL093173, 2021. doi: <https://doi.org/10.1029/2021GL093173>. URL <https://agupubs.onlinelibrary.wiley.com/doi/abs/10.1029/2021GL093173> e2021GL093173 2021GL093173.

[25] Primož Kajdič, Xóchitl Blanco-Cano, Lucile Turc, Martin Archer, Savvas Raptis, Terry Z. Liu, Yann Pfau-Kempf, Adrian T. LaMoury, Yufei Hao, Philippe C. Escoubet, Nojan Omidi, David G. Sibeck, Boyi Wang, Hui Zhang, and Yu Lin. Transient upstream mesoscale structures: drivers of solar-quiet space weather. *Frontiers in Astronomy and Space Sciences*, 11:1436916, July 2024. doi: 10.3389/fspas.2024.1436916.

[26] H. Madanian, N. Omidi, D. G. Sibeck, L. Andersson, R. Ramstad, S. Xu, J. R. Gruesbeck, S. J. Schwartz, R. A. Frahm, D. A. Brain, P. Kajdic, F. G. Eparvier, D. L. Mitchell, and S. M. Curry. Transient Foreshock Structures Upstream of Mars: Implications of the Small Martian Bow Shock. *Geophysical Research Letters*, 50(8):e2022GL101734, April 2023. doi: 10.1029/2022GL101734.

[27] K. Meziane and C. D'Uston. A statistical study of the upstream intermediate ion boundary in the Earth's foreshock. *Annales Geophysicae*, 16(2):125–133, February 1998. doi: 10.1007/s00585-998-0125-7.

[28] Karim Meziane, M. Wilber, C. Mazelle, G. K. Parks, and A. M. Hamza. A review of field-aligned beams observed upstream of the bow shock. In Gang Li, Gary P. Zank, and C. T. Russell, editors, *The Physics of Collisionless Shocks: 4th Annual IGPP International Astrophysics Conference*, volume 781 of *American Institute of Physics Conference Series*, pages 116–122. AIP, August 2005. doi: 10.1063/1.2032683.

[29] M. Neugebauer, D. R. Clay, B. E. Goldstein, B. T. Tsurutani, and R. D. Zwickl. A reexamination of rotational and tangential discontinuities in the solar wind. *Journal of Geophysical Research: Space Physics*, 89(A7):5395–5408, 1984. doi: <https://doi.org/10.1029/JA089iA07p05395>. URL <https://agupubs-onlinelibrary-wiley-com.pbidi.unam.mx:2443/doi/abs/10.1029/JA089iA07p05395>.

[30] N. Omidi and D. G. Sibeck. Formation of hot flow anomalies and solitary shocks. *J. Geophys. Res.*, 112:A01203, January 2007. doi: 10.1029/2006JA011663.

- [31] N. Omidi and D. Winske. Steepening of kinetic magnetosonic waves into shocklets: Simulations and consequences for planetary shocks and comets. *Journal of Geophysical Research: Space Physics*, 95(A3):2281–2300, 1990. doi: <https://doi.org/10.1029/JA095iA03p02281>. URL <https://agupubs.onlinelibrary.wiley.com/doi/abs/10.1029/JA095iA03p02281>.
- [32] N. Omidi, D. G. Sibeck, and X. Blanco-Cano. Foreshock compressional boundary. *J. Geophys. Res.*, 114:A08205, August 2009. doi: 10.1029/2008JA013950.
- [33] N. Omidi, J. P. Eastwood, and D. G. Sibeck. Foreshock bubbles and their global magnetospheric impacts. *J. Geophys. Res.*, 115:A06204, June 2010. doi: 10.1029/2009JA014828.
- [34] N. Omidi, D. Sibeck, X. Blanco-Cano, D. Rojas-Castillo, D. Turner, H. Zhang, and P. Kajdič. Dynamics of the foreshock compressional boundary and its connection to foreshock cavities. *J. Geophys. Res.*, 118:823–831, February 2013. doi: 10.1002/jgra.50146.
- [35] N. Omidi, H. Zhang, D. Sibeck, and D. Turner. Spontaneous hot flow anomalies at quasi-parallel shocks: 2. hybrid simulations. *Journal of Geophysical Research: Space Physics*, 118(1):173–180, 2013. ISSN 2169-9402. doi: 10.1029/2012JA018099. URL <http://dx.doi.org/10.1029/2012JA018099>.
- [36] N. Omidi, G. Collinson, and D. Sibeck. Foreshock bubbles at venus: Hybrid simulations and vex observations. *Journal of Geophysical Research: Space Physics*, 125(2):e2019JA027056, 2020. doi: <https://doi.org/10.1029/2019JA027056>. URL <https://agupubs.onlinelibrary.wiley.com/doi/abs/10.1029/2019JA027056>. e2019JA027056 2019JA027056.
- [37] N. Omidi, S. H. Lee, D. G. Sibeck, D. L. Turner, T. Z. Liu, and V. Angelopoulos. Formation and topology of foreshock bubbles. *Journal of Geophysical Research: Space Physics*, 125(9):e2020JA028058, 2020. doi: <https://doi.org/10.1029/2020JA028058>. URL <https://agupubs.onlinelibrary.wiley.com/doi/abs/10.1029/2020JA028058>. e2020JA028058 2020JA028058.
- [38] N. Omidi, S. H. Lee, and D. G. Sibeck. Ion Acceleration by Foreshock Bubbles. *Journal of Geophysical Research (Space Physics)*, 126(5):e28924, May 2021. doi: 10.1029/2020JA028924.
- [39] G. Paschmann, N. Sckopke, J.R. Asbridge, S.J. Bame, and J.T. Gosling. Energization of solar wind ions by reflection from the earth's bow shock. *Journal of Geophysical Research: Space Physics*, 85(A9):4689–4693, 1980. doi: <https://doi.org/10.1029/JA085iA09p04689>. URL <https://agupubs.onlinelibrary.wiley.com/doi/abs/10.1029/JA085iA09p04689>.
- [40] G. Paschmann, N. Sckopke, I. Papamastorakis, J. R. Asbridge, S. J. Bame, and J. T. Gosling. Characteristics of reflected and diffuse ions upstream from the earth's bow shock. *Journal of Geophysical Research*, 86(A6):4355–4364, June 1981. doi: 10.1029/JA086iA06p04355.
- [41] G. Paschmann, G. Haerendel, N. Sckopke, E. Möbius, H. Lühr, and C. W. Carlson. Three-dimensional plasma structures with anomalous flow directions near the earth's bow shock. *Journal of Geophysical Research: Space Physics*, 93(A10):

11279–11294, 1988. doi: <https://doi.org/10.1029/JA093iA10p11279>. URL <https://agupubs.onlinelibrary.wiley.com/doi/abs/10.1029/JA093iA10p11279>.

[42] C. Pollock, T. Moore, A. Jacques, J. Burch, U. Giiese, Y. Saito, T. Omoto, L. Avanov, A. Barrie, V. Coffey, J. Dorelli, D. Gershman, B. Giles, T. Rosnack, C. Salo, S. Yokota, M. Adrian, C. Aoustin, C. Auletti, S. Aung, V. Bigio, N. Cao, M. Chandler, D. Chornay, K. Christian, G. Clark, G. Collinson, T. Corris, A. De Los Santos, R. Devlin, T. Diaz, T. Dickerson, C. Dickson, A. Diekmann, F. Diggs, C. Duncan, A. Figueroa-Vinas, C. Firman, M. Freeman, N. Galassi, K. Garcia, G. Goodhart, D. Guererro, J. Hageman, J. Hanley, E. Hemminger, M. Holland, M. Hutchins, T. James, W. Jones, S. Kreisler, J. Kujawski, V. Lavu, J. Lobell, E. LeCompte, A. Lukemire, E. MacDonald, A. Mariano, T. Mukai, K. Narayanan, Q. Nguyan, M. Onizuka, W. Paterson, S. Persyn, B. Piepgrass, F. Cheney, A. Rager, T. Raghuram, A. Ramil, L. Reichenthal, H. Rodriguez, J. Rouzaud, A. Rucker, Y. Saito, M. Samara, J. A. Sauvaud, D. Schuster, M. Shappirio, K. Shelton, D. Sher, D. Smith, K. Smith, S. Smith, D. Steinfeld, R. Szymkiewicz, K. Tanimoto, J. Taylor, C. Tucker, K. Tull, A. Uhl, J. Vloet, P. Walpole, S. Weidner, D. White, G. Winkert, P. S. Yeh, and M. Zeuch. Fast plasma investigation for magnetospheric multiscale. *Space Science Reviews*, 199(1):331–406, 2016. doi: 10.1007/s11214-016-0245-4. URL <https://doi.org/10.1007/s11214-016-0245-4>.

[43] H. Rème, C. Aoustin, J. M. Bosqued, I. Dandouras, B. Lavraud, J. A. Sauvaud, A. Barthe, J. Bouyssou, Th. Camus, O. Coeur-Joly, A. Cros, J. Cuvilo, F. Ducay, Y. Garbarowitz, J. L. Medale, E. Penou, H. Perrier, D. Romefort, J. Rouzaud, C. Vallat, D. Alcaydé, C. Jacquay, C. Mazelle, C. D'Uston, E. Möbius, L. M. Kistler, K. Crocker, M. Granoff, C. Mouikis, M. Popecki, M. Vosbury, B. Klecker, D. Hovestadt, H. Kucharek, E. Kuenneth, G. Paschmann, M. Scholer, N. Sckopke, J. E. Seidenschwang, C. W. Carlson, D. W. Curtis, C. Ingraham, R. P. Lin, J. P. McFadden, G. K. Parks, T. Phan, V. Formisano, E. Amata, M. B. Bavassano-Cattaneo, P. Baldetti, R. Bruno, G. Chionchio, A. di Lellis, M. F. Marcucci, G. Pallocchia, A. Korth, P. W. Daly, B. Graeve, H. Rosenbauer, V. Vasyliunas, M. McCarthy, M. Wilber, L. Eliasson, R. Lundin, S. Olsen, E. G. Shelley, S. Fuselier, A. G. Ghielmetti, W. Lennartsson, C. P. Escoubet, H. Balsiger, R. Friedel, J. B. Cao, R. A. Kovrazhkin, I. Papamastorakis, R. Pellat, J. Scudder, and B. Sonnerup. First multispacecraft ion measurements in and near the Earth's magnetosphere with the identical Cluster ion spectrometry (CIS) experiment. *Annales Geophysicae*, 19:1303–1354, October 2001. doi: 10.5194/angeo-19-1303-2001.

[44] D. Rojas-Castillo, X. Blanco-Cano, P. Kajdič, and N. Omidi. Foreshock compressional boundaries observed by Cluster. *Journal of Geophysical Research: Space Physics*, 118:698–715, February 2013. doi: 10.1029/2011JA017385.

[45] C. T. Russell, B. J. Anderson, W. Baumjohann, K. R. Bromund, D. Dearborn, D. Fischer, G. Le, H. K. Leinweber, D. Leneman, W. Magnes, J. D. Means, M. B. Moldwin, R. Nakamura, D. Pierce, F. Plaschke, K. M. Rowe, J. A. Slavin, R. J. Strangeway, R. Torbert, C. Hagen, I. Jernej, A. Valavanoglou, and I. Richter. The magnetospheric multiscale magnetometers. *Space Science Reviews*, 199(1):189–256, 2016. doi: 10.1007/s11214-014-0057-3. URL <https://doi.org/10.1007/s11214-014-0057-3>.

[46] Manfred Scholer. Upstream waves, shocklets, short large-amplitude magnetic

structures and the cyclic behavior of oblique quasi-parallel collisionless shocks. *Journal of Geophysical Research*, 98(A1):47–58, January 1993. doi: 10.1029/92JA01875.

[47] S. J. Schwartz. *Shock and Discontinuity Normals, Mach Numbers, and Related Parameters*, volume 1 of *ISSI Scientific Reports Series*, ESA/ISSI. 1998.

[48] S. J. Schwartz, G. Paschmann, N. Sckopke, T. M. Bauer, M. Dunlop, A. N. Fazakerley, and M. F. Thomsen. Conditions for the formation of hot flow anomalies at Earth’s bow shock. *J. Geophys. Res.*, 105:12639–12650, June 2000. doi: 10.1029/1999JA000320.

[49] Xiao-Chen Shen, Quanqi Shi, Boyi Wang, Hui Zhang, Mary K. Hudson, Yukitoshi Nishimura, Michael D. Hartinger, Anmin Tian, Qiu-Gang Zong, I. J. Rae, and Alexander W. Degeling. Dayside magnetospheric and ionospheric responses to a foreshock transient on 25 june 2008: 1. flr observed by satellite and ground-based magnetometers. *Journal of Geophysical Research: Space Physics*, 123(8):6335–6346, 2018. doi: <https://doi.org/10.1029/2018JA025349>. URL <https://agupubs.onlinelibrary.wiley.com/doi/abs/10.1029/2018JA025349>.

[50] D. G. Sibeck, N. L. Borodkova, S. J. Schwartz, C. J. Owen, R. Kessel, S. Kokubun, R. P. Lepping, R. Lin, K. Liou, H. Lühr, R. W. McEntire, C.-I. Meng, T. Mukai, Z. Nemecek, G. Parks, T. D. Phan, S. A. Romanov, J. Safrankova, J.-A. Sauvaud, H. J. Singer, S. I. Solovyev, A. Szabo, K. Takahashi, D. J. Williams, K. Yumoto, and G. N. Zastenker. Comprehensive study of the magnetospheric response to a hot flow anomaly. *J. Geophys. Res.*, 104:4577–4594, March 1999. doi: 10.1029/1998JA900021.

[51] D. G. Sibeck, T.-D. Phan, R. Lin, R. P. Lepping, and A. Szabo. Wind observations of foreshock cavities: A case study. *J. Geophys. Res.*, 107:1271, October 2002. doi: 10.1029/2001JA007539.

[52] D. G. Sibeck, N. Omidi, I. Dandouras, and E. Lucek. On the edge of the foreshock: model-data comparisons. *Ann. Geophys.*, 26:1539–1544, June 2008. doi: 10.5194/angeo-26-1539-2008.

[53] D. G. Sibeck, S. H. Lee, N. Omidi, and V. Angelopoulos. Foreshock Cavities: Direct Transmission Through the Bow Shock. *Journal of Geophysical Research (Space Physics)*, 126(5):e29201, May 2021. doi: 10.1029/2021JA029201.

[54] J. A. Slavin and R. E. Holzer. Solar wind flow about the terrestrial planets, 1. Modeling bow shock position and shape. *Journal of Geophysical Research*, 86 (A13):11401–11418, December 1981. doi: 10.1029/JA086iA13p11401.

[55] A. V. Suvorova, A. V. Dmitriev, V. A. Parkhomov, and B. Tsegmed. Quiet Time Structured Pc1 Waves Generated During Transient Foreshock. *Journal of Geophysical Research (Space Physics)*, 124(11):9075–9093, November 2019. doi: 10.1029/2019JA026936.

[56] Lucile Turc, Martin O. Archer, Hongyang Zhou, Yann Pfau-Kempf, Jonas Suni, Primož Kajdič, Xóchitl Blanco-Cano, Souhail Dahani, Markus Battarbee, Savvas Raptis, Terry Z. Liu, Hui Zhang, C. Philippe Escoubet, Adrian T. LaMoury, Shi Tao, Veera Lipsanen, Yufei Hao, and Minna Palmroth. Interplay between a foreshock bubble and a hot flow anomaly forming along the same rotational

discontinuity. *Geophysical Research Letters*, 52(12):e2025GL116473, 2025. doi: <https://doi.org/10.1029/2025GL116473>. URL <https://agupubs.onlinelibrary.wiley.com/doi/abs/10.1029/2025GL116473>. e2025GL116473 2025GL116473.

[57] Boyi Wang, Yukitoshi Nishimura, Hui Zhang, Xiao-Chen Shen, Larry Lyons, Vassilis Angelopoulos, Yusuke Ebihara, Allan Weatherwax, Andrew J. Gerrard, and Harald U. Frey. The 2-d structure of foreshock-driven field line resonances observed by the THEMIS satellite and ground-based imager conjunctions. *Journal of Geophysical Research: Space Physics*, 124(8):6792–6811, 2019. doi: <https://doi.org/10.1029/2019JA026668>. URL <https://agupubs.onlinelibrary.wiley.com/doi/abs/10.1029/2019JA026668>.

[58] D. Winske and M. M. Leroy. Diffuse ions produced by electromagnetic ion beam instabilities. *Journal of Geophysical Research: Space Physics*, 89(A5): 2673–2688, 1984. doi: <https://doi.org/10.1029/JA089iA05p02673>. URL <https://agupubs.onlinelibrary.wiley.com/doi/abs/10.1029/JA089iA05p02673>.

[59] D. T. Young, J. L. Burch, R. G. Gomez, A. De Los Santos, G. P. Miller, P. Wilson, N. Paschalidis, S. A. Fuselier, K. Pickens, E. Hertzberg, C. J. Pollock, J. Scherrer, P. B. Wood, E. T. Donald, D. Aaron, J. Furman, D. George, R. S. Gurnee, R. S. Hourani, A. Jacques, T. Johnson, T. Orr, K. S. Pan, S. Persyn, S. Pope, J. Roberts, M. R. Stokes, K. J. Trattner, and J. M. Webster. Hot Plasma Composition Analyzer for the Magnetospheric Multiscale Mission. *Space Science Reviews*, 199(1-4): 407–470, March 2016. doi: 10.1007/s11214-014-0119-6.

[60] Hui Zhang and Qiugang Zong. *Transient Phenomena at the Magnetopause and Bow Shock and Their Ground Signatures*, chapter 2, pages 11–37. American Geophysical Union (AGU), 2020. ISBN 9781119509592. doi: <https://doi.org/10.1002/9781119509592.ch2>. URL <https://agupubs.onlinelibrary.wiley.com/doi/abs/10.1002/9781119509592.ch2>.